RESEARCH ARTICLE
SPACE PHYSICS: MAGNETOSPHERIC PHYSICS

Earth and Planetary Physics
5: 19–31, 2021
doi: 10.26464/epp2021007

An updated constraint on the local stratigraphy at the Chang'E-4 landing site

YiRen Chang[1], ZhiYong Xiao[2,3]*, YiChen Wang[2], ChunYu Ding[2], Jun Cui[2,3,4], and YuZhen Cai[2]

[1]State Key Laboratory of Lunar and Planetary Sciences, Macau University of Science and Technology, Macau 999078, China;

[2]Planetary Environmental and Astrobiological Research Laboratory, School of Atmospheric Sciences, Sun Yat-sen University, Zhuhai, Guangdong 519000, China;

[3]Center for Excellence in Comparative Planetology, Chinese Academy of Sciences, Hefei 230000, China;

[4]National Astronomical Observations of China, Chinese Academy of Sciences, Beijing 100000, China

Key Points:

- Detailed crater statistics were performed for key stratigraphic markers at the Chang'E-4 landing region.
- Alder is older than the mare basalts at the landing site, and Finsen is the youngest.
- Minor contributions of ejecta by Alder should exist at the shallow subsurface.

Citation: Chang, Y. R., Xiao, Z. Y., Wang, Y. C., Ding, C. Y., Cui, J. and Cai, Y. Z. (2021). An updated constraint on the local stratigraphy at the Chang'E-4 landing site. *Earth Planet. Phys.*, *5*(1), 19–31. http://doi.org/10.26464/epp2021007

Abstract: The Chang'E-4 mission has been exploring the lunar farside. Two scientific targets of the rover onboard are (1) resolving the possible mineralogy related to the South Pole-Aitken basin and (2) understanding the subsurface processes at the lunar farside. Publications to date that are based on the reflectance spectra and radar data obtained by the rover have shown a persistent inconsistency about the local stratigraphy. To explain both the abnormal surface topography at the landing site and the unexpected radargram observed by the rover, the Alder crater has been frequently reported to be older than the mare basalts at that landing site. However, this argument is not supported by earlier geological mapping nor recent crater statistics. Resolving this controversy is critical for a full understanding of the geological history of the landing area and for correct interpretations of the scientific data returned. Employing detailed crater statistics, rigorous statistical analyses, and an updated crater chronology function, this study is determined to resolve the relative ages of the Alder crater, Finsen crater, and the mare basalts on the floor of Von Kármán. Our results reveal that while background secondaries and local resurfacing have widely occurred in the study area, affecting age determinations, the statistics are significant enough to conclude that the Alder crater is the oldest among the three targets. This independent constraint is consistent with both the crosscutting relationships of different terrains in this area and global stratigraphic mapping. Our results exclude Alder as a possible contributor of the post-mare deposits at the landing site, appealing for a more systematic stratigraphy study to resolve the provenances of these deposits.

Keywords: Moon; Chang'E-4; impact craters; absolute model age; stratigraphy

1. Introduction

The Chang'E-4 mission, consisting of a relay satellite, a lander, and a rover, has been successfully deployed to the floor of the Von Kármán crater (diameter D = 185 km; 46.4°S, 176.5°E). The landing area is located within the South Pole-Aitken (SPA) basin (Wu WR et al., 2017), which is the largest impact structure on the Moon. The formation of the SPA basin has excavated ancient lunar crustal and even upper mantle materials (Potter et al., 2012). However, the possible composition of the lunar mantle has been elusive in previous studies that were based on orbital composition data and numerical simulations of the SPA impact (Melosh et al., 2017). Two important reasons for the debates are that (1) simulations of large impact basins depend heavily on unconstrained parameters, and (2) interpretations of planetary remote sensing normally have multiplicity. Therefore, sampling the SPA has been a high priority target for furture surface explorations on the Moon.

A key scientific target of the Chang'E-4 mission (CE-4) is to explore the composition of surface materials within the SPA, finding information that might be traced to possible mantle materials excavated by this ancient basin (Wu WR et al., 2017). However, this is not a straightforward task. Besides the ambiguous initial crustal configuration after the SPA basin was formed (e.g., whether or not the hypothesized thick melt sheet has been differentiated), post-impact modification has been extensive, as numerous impact basins and multiple episodes of volcanic eruptions have occurred at different places within the SPA (Moriarty III and Pieters, 2018). Resolving the provenance of surface materials and detecting the

Correspondence to: Z. Y. Xiao, xiaozhiyong@mail.sysu.edu.cn
Received 25 AUG 2020; Accepted 27 OCT 2020.
Accepted article online 25 DEC 2020.

primordial materials formed by the SPA is critical to finding the mantle materials that were excavated.

Based on reflectance spectra returned by the rover, most interpretations have suggested that the surface regolith is enriched in calcium-rich pyroxenes, and that olivine is a minor component (Lin HL et al., 2020; Ma P et al., 2020; Huang J et al., 2020), which are consistent with orbital observations (Huang J et al., 2018; Ling ZC et al., 2019). An obvious impact ray is visible at the landing site, which was delivered by the Finsen crater (D = 73 km; 42.3°S, 177.7°W) to the northeast of Von Kármán. Therefore, the provenance of the surface regolith is usually ascribed to the distal ejecta delivered by Finsen (Figure 1). On the other hand, morphological studies have shown that the entire landing area has been occupied by secondaries with various sizes and degradation states, which were delivered by craters from different directions (Huang J et al., 2018). Mixing of surface materials should be pronounced (Figure 1c), which is evident by the different compositions exposed from various depths by relatively large impact craters (Huang J et al., 2018; Li CL et al., 2019). Indeed, both basaltic (Huang J et al., 2020) and feldspathic rocky fragments (Ma P et al., 2020) have been found by the rover. Therefore, understanding the major source(s) of regolith at the landing site is critically important to interpret the compositional data returned. Specifically, besides Finsen, which other crater(s) contributed additional ejecta to the post-mare deposits?

Following the first successful exterrestrial ground-penetrating radar, performed by the Chang'E-3 mission (Xiao L et al., 2015; Fa WZ et al., 2015; Zhang JH et al., 2015), the Yutu-2 rover of Chang'

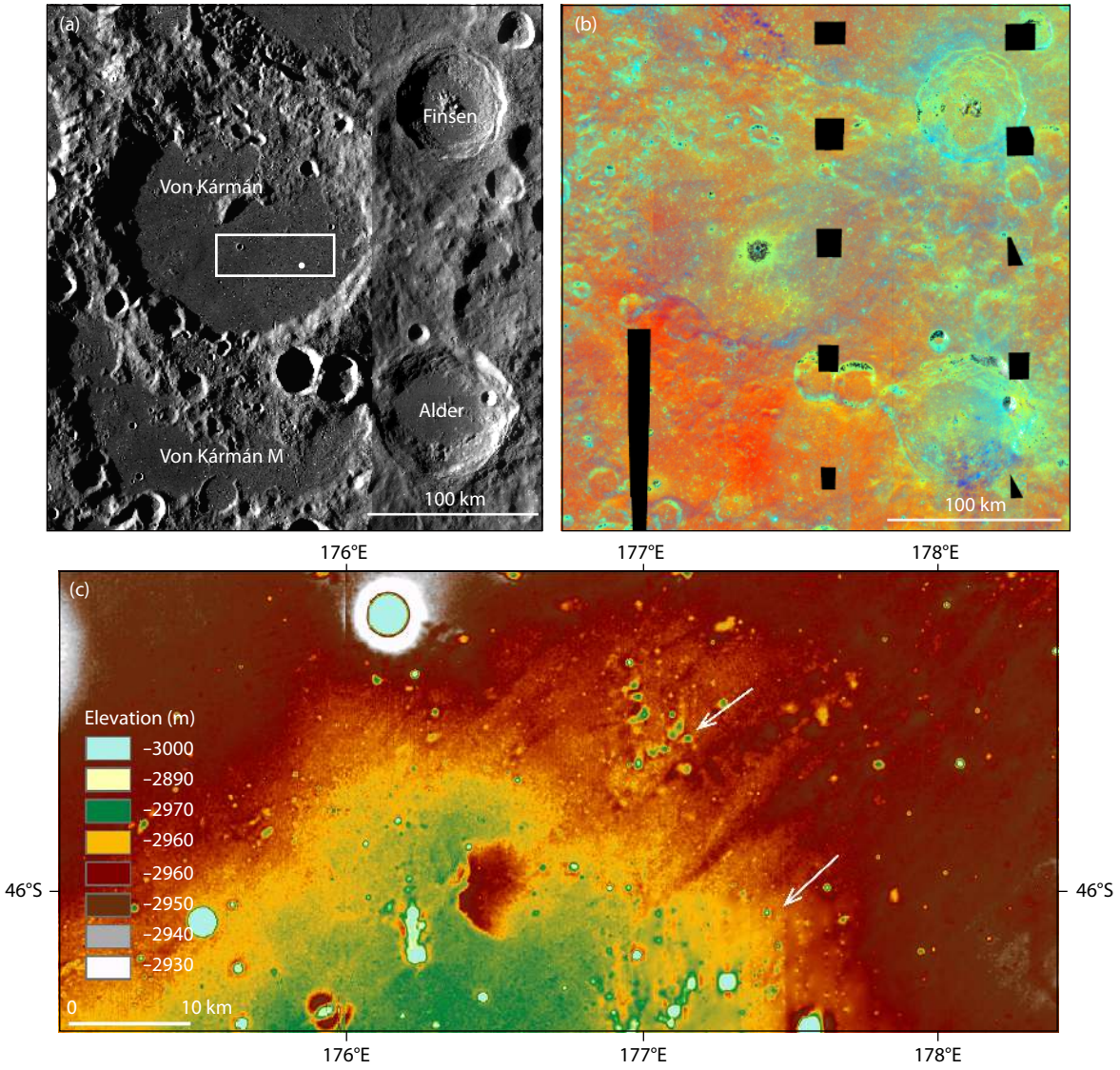

Figure 1. Geological context of the Chang'E-4 landing area and the landing site is marked as a white circle. (a) The landing area is located on a mare unit, and key craters in the surrounding area are denoted in white. The central coordinates of this area are 46°S, 178°E. (b) Composition and maturity difference of materials in the landing area and impact rays delivered by the Finsen crater are the blueish diffuse materials. (c) The regional topography of the landing site is dominated by the northeast-to-southwest-trending lineations that were formed by the Finsen crater. Note that numerous younger secondaries are visible in this map, e.g., white arrows. The location of this area is denoted as the white box in panel (a).

E-4 is equipped with a similar payload to investigate the propagation of electromagnetic waves in lunar farside materials. A scientific target is to understand the formation of regolith at the lunar farside. In the radargram obtained, materials deeper than ~40–45 m are believed to be mare basalts that filled in the floor of Von Kármán; materials shallower than ~10–13 m (Lai JL et al., 2019, 2020; Li CL et al., 2020; Ding CY et al., 2020; Zhang L et al., 2020) have dielectric properties similar to typical lunar regolith.

The possible provenance of the >~40 m thick porous deposits is obscure, and widespread discrepancies exist in the interpretations. Referring to published stratigraphic ages of impact structures around the landing site (Figure 1a), earlier studies predicted that Finsen was the major contributor of the post-mare deposits (Li CL et al., 2019). Employing an analytical model for the thickness of impact ejecta as a function of radial distances to the parent crater, the total thickness of ejecta delivered to the landing site by all significant post-mare craters is less than 14 meters (Huang J et al., 2018; Lai JL et al., 2020). However, numerical simulations for the formation of Finsen- and Alder-sized craters predicted an ejecta thickness of > 60 meters at the landing sites (Di KC et al., 2019), which is much larger than the thickness of post-mare deposits observed by the lunar penetrating radar (Lai JL et al., 2019; Lai JL et al., 2020; Li CL et al., 2020). On the other hand, the thickness of post-mare deposits constrained by the radargram is consistent with orbital observations, which were based on the reflectance spectra of small craters that have exposed subsurface mare basalts (Huang J et al., 2018; Ling ZC et al., 2019; Li CL et al., 2019). After scanning all the possible source craters that may have delivered ejecta to the landing site (Huang J et al., 2018; Lai JL et al., 2020), the key question now is whether Alder is older or younger than the mare basalts at the landing site (Figure 1a).

The above literature review summarizes the key question targeted in this paper, which is to resolve the relative ages of the Alder crater, the Finsen crater, and the mare basalts on the floor of Von Kármán. While we are aware that earlier studies (Ivanov et al., 2018; Pasckert et al., 2018; Huang J et al., 2018; Ling ZC et al., 2019; Gou S et al., 2020; Lu et al., 2021) have tried to estimate the model ages for some of our targets via crater statistics, this paper is built on more focused studies of various crater populations for each of the targets. Strictly following technical suggestions to perform crater counts (Michael and Neukum, 2010) and analyze crater size-frequency distributions (SFD; Robbins et al., 2018), we avoid caveats known to the crater count community, such as obvious secondaries (Xiao ZY and Strom, 2012; Xiao ZY, 2018), image resolution (Wang YC et al., 2020), and slopes (Xiao ZY et al., 2013). Multiple counting areas are selected based on photogeology study for each of the targets, and crater populations at various diameter ranges are studied.

2. Data and Method

Different versions of global mosaics obtained by the Lunar Reconnaissance Orbiter Camera (LROC; Robinson et al., 2010) and Wide Angle Camera (WAC; 100 m/pixel) are used as the base map to study the regional context. Images obtained by the Kaguya Terrain Camera (TC; Haruyama et al., 2008) are used to analyze the morphology of local areas. The LOLA digital elevation model coregistered with SELENE data (SLDEM; 59 m/pixel; Barker et al., 2016) is employed to analyze the topography (Barker et al., 2016). Materials with different compositions and/or preservation states are differentiated based on the Clementine Ultraviolet–Visible global mosaic (Eliason et al., 1999). All single frame imagery data are calibrated using the USGS Integrated Software for Imagers and Spectrometers (http://isis.astrogeology.usgs.gov/) following the standard process procedure. Table S1 summarizes the data sources used in this study.

Selection of counting areas was based on the above data, following the guidance introduced by Michael and Neukum (2010). Continuous ejecta deposits and possible melt pools on both crater rims and crater floors were taken as the counted areas. The counting areas voided complicated topographies and shadows, and each counting area is homogeneous in terms of surface morphology (Xiao ZY et al., 2013). Both the interiors and exteriors of Alder and Finsen have been heavily contaminated by secondaries (section 3), similar to the situation on the mare surface in Von Kármán (Huang J et al., 2018). Therefore, during the selection of counting areas, we were limited by small sizes of ideal counting areas. To enhance statistical significance, we also selected larger areas that include shallow slope regions, but only craters that are much larger than half of the topographic wavelength are included, so that potential negative influences caused by mass movements are avoided (Xiao ZY et al., 2013). This approach allows us to perform cross comparisons of results derived for multiple counting areas of a single target. Table S2 in the appendix shows detailed information of the counting areas.

To avoid incomplete recognition, images with a solar incidence angle of > 60° were used to collect craters in the counting areas (Ostrach et al., 2011). Table S3 shows information of the base images used for the counts. The crater counts were performed by exhaustive searching of craters larger than 3 pixels of the base image, but only craters larger than 10 pixels are considered completely included (Wang YC et al., 2020). The counting process has excluded obvious chains and clusters of secondaries (McEwen and Bierhaus, 2006; Xiao ZY and Strom, 2012).

The novel technique of analyzing crater size-frequency distribution (SFD) advocated by Robbins et al. (2018) is used here. A Gaussian kernel density estimator (i.e. KDE) is used to derive the crater SFD, and the mean value and bandwidth of the KDE are the measured crater diameter (D) and 0.1D, respectively. The hybrid-bootstrap method is used to estimate the 2σ confidence intervals of the SFD (Robbins et al., 2018). Compared to traditional methods of analyzing crater SFD, the new technique is more rigorous in terms of statistic reliability (Robbins et al., 2018). The dedicated crater counts performed here are characterized by small samples of usable craters (Section 3), because shadows normally occupy large areas of images obtained for such high latitude areas, and abundant secondaries are recognized in these areas, limiting both the size of usable counting areas and the number of usable craters (Section 3). The advantage of this new statistical technique is especially apparent for such small samples. The crater chronology function proposed by Robbins (2014) is updated from that of Neukum et al. (2001), and it is used here together with the production function proposed by Neukum et al. (2001) to derive the absolute model ages.

3. Results

3.1 Crater Size-Frequency Distribution at the Finsen Crater

Finsen is a typical complex crater that features faint impact rays (Figure 1b). It has been taken as a Copernican-aged crater (Ling et al., 2018), but the preservation of impact rays is not strictly correlated with the stratigraphic age of the parent crater (Hawke et al., 2004). In geologic maps published by both Wilhelms et al. (1979) and Fortezzo et al. (2020), Finsen was mapped as an Eratosthenian-aged crater. Previous crater counts for Finsen (Ivanov et al., 2018; Gou et al., 2020) yielded a model age of ~3.5 billion years (Ga), which is not so different compared to the ~3.6 Ga old mare basalts in the floor of Von Kármán (Huang J et al., 2018; Ling ZC et al., 2019; Pasckert et al., 2015). After the submission of this paper, a new publication on the model age of Finsen emerged, which was based on crater counts on the southern floor and ejecta, yielding numbers of ~3.0 and 3.1 Ga, respectively (Lu et al., 2021).

We take two strategies of crater statistics to investigate the model age of the Finsen crater. Four populations of relatively large craters at several locations of both the continuous ejecta deposits and crater floors are selected (Figure 2), and 7 populations of relatively small impact craters on several smaller areas are selected (Figure 3). The two sets of crater populations are complementary to each other, as they cover different diameter ranges. Therefore, possible contributions caused by background secondaries (Xiao ZY, 2018) and heterogeneous resurfacing processes can be investigated. A ~30 km diameter is located on the northeastern crater rim of Finsen (Figure 1a), so its secondaries and the impact-induced resurfacing have heavily affected nearby regions. Therefore, the selected counting areas are away from the northern and eastern rims, and craters on the floor of Finsen are used with special cautions (Figures 2 and 3).

The absolute model ages derived from the four populations of relatively large craters and those derived from the seven populations of relatively small craters are shown in Figures 4 and 5, respectively. The results differ from each other by a maximum factor of > 2, i.e., the D > 0.4 km small crater population on the crater floor (Figure 5c) versus the D > 0.15–0.45 km crater populations on the continuous ejecta deposits (Figure 5a). Within error bars, most model ages of the 11 populations are around ~2.0 Ga (Figures 4c, 4d, 5b and 5d). The population of relatively large craters on the crater floor yields a comparable model age with that derived by Lu et al. (2021), Gou et al. (2020), and Ivanov et al. (2018), testifying a good repeatability of our crater collection. In conclusion, the majority of the absolute ages modelled for Finsen are less than 3.0 Ga.

3.2 Crater Size-Frequency Distribution at the Alder Crater

The overlapping relationship between ejecta formed by Finsen and Alder suggests that Finsen is younger than Alder, which is consistent with the updated geologic map (Fortezzo et al., 2020; Figure 6b). Considering the short distance between Finsen and Alder, the Finsen impact has substantially modified the northern rim and floor of Alder, evidenced by the strong modification of the mare basalts on the floor of Von Kármán caused by Finsen's ejecta (Figure 1c). Therefore, we select counting areas that are

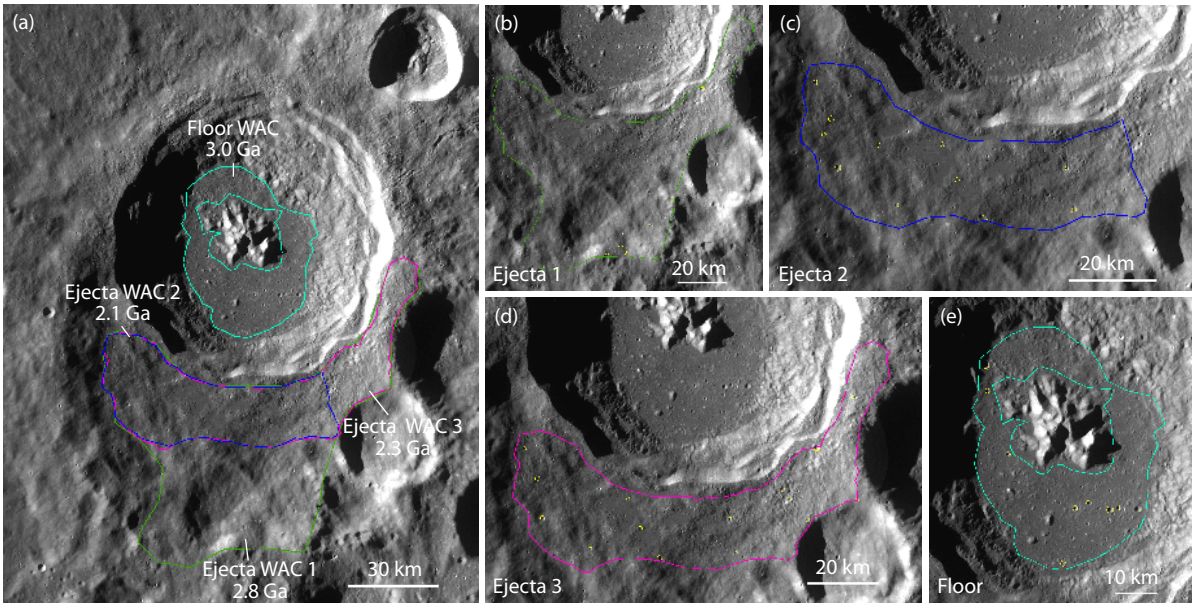

Figure 2. Collections of relatively large craters on the continuous ejecta deposits and floor of Finsen. Panel (a) shows the locations of the counting areas, and panels (b)–(e) show the detailed morphology of the counting areas and craters used to estimate absolute model ages. Craters as small as several pixels were included in counts, but only those larger than chains and clusters of obvious secondaries are used to derive the crater densities (marked as yellow circles). For crater populations collected in panels (b)–(e), the minimum diameter used for age determination is 1.1, 0.7, 0.7 and 0.8 km, respectively. Names of the counting areas are denoted nearby, and WAC means that the count was based on LROC WAC mosaics.

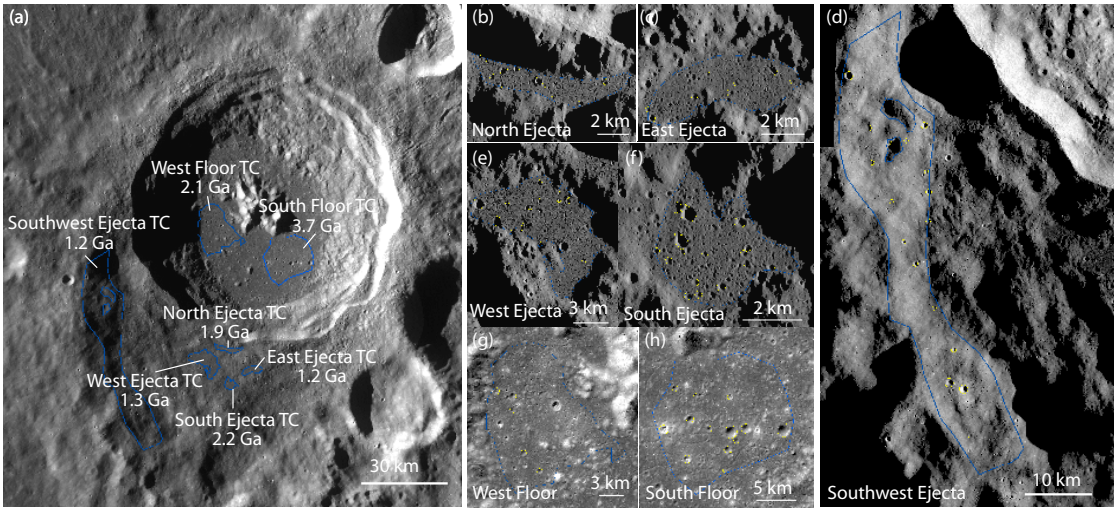

Figure 3. Collections of relatively small craters on the continuous ejecta deposits and floor of Finsen. Panel (a) shows the locations of the counting areas, and panels (b)–(h) show the detailed morphology of the counting areas and craters used to estimate absolute model ages. Craters as small as several pixels were included in counts, but only those larger than chains and clusters of obvious secondaries are used to derive the crater densities (marked as yellow circles). For crater populations collected in (b)–(h), the minimum diameter used for age determination is 0.14, 0.15, 0.45, 0.2, 0.15, 0.5, and 0.4 km, respectively. Names of the counting areas are denoted nearby; TC means the count was based on Kaguya TC images.

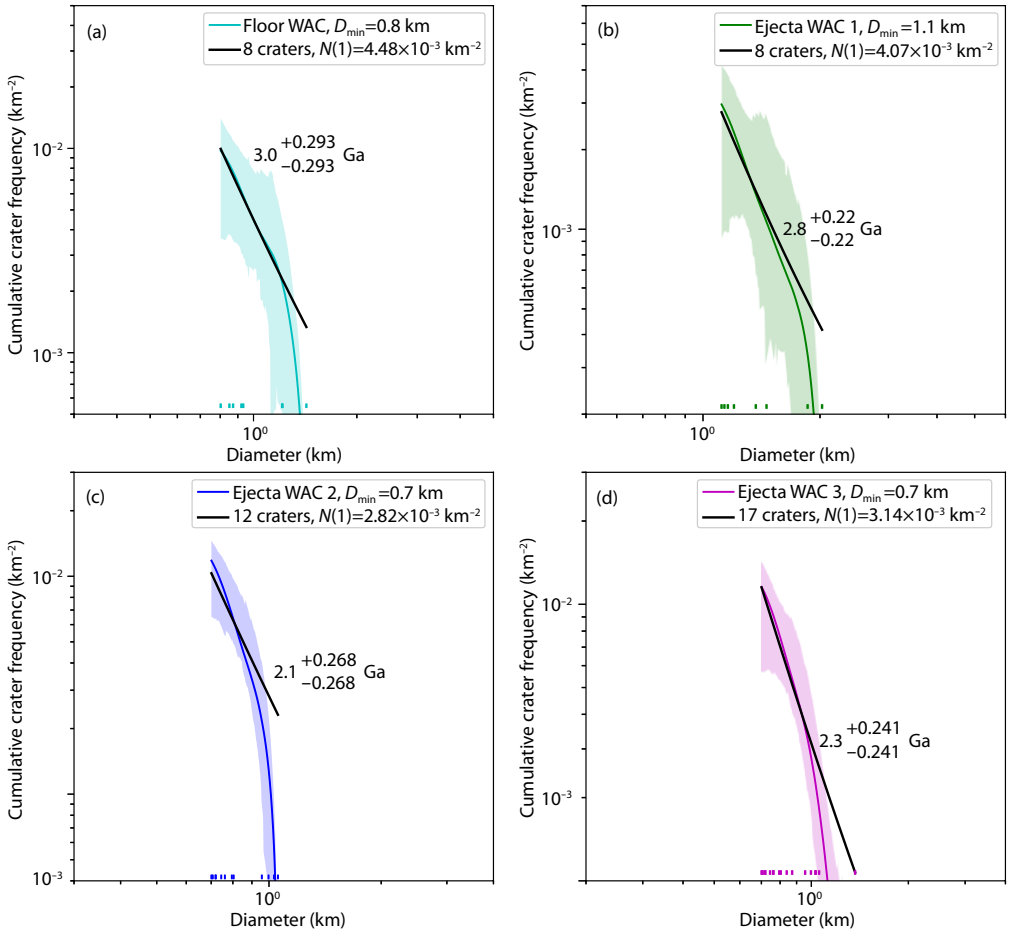

Figure 4. Cumulative crater size-frequency distribution and absolute model ages for the four populations of relatively large craters collected on the crater floor and ejecta deposits of Finsen. The colors and names of the counting areas correspond to those shown in Figure 2. Shaded colors are the errors for the crater size-frequency distributions.

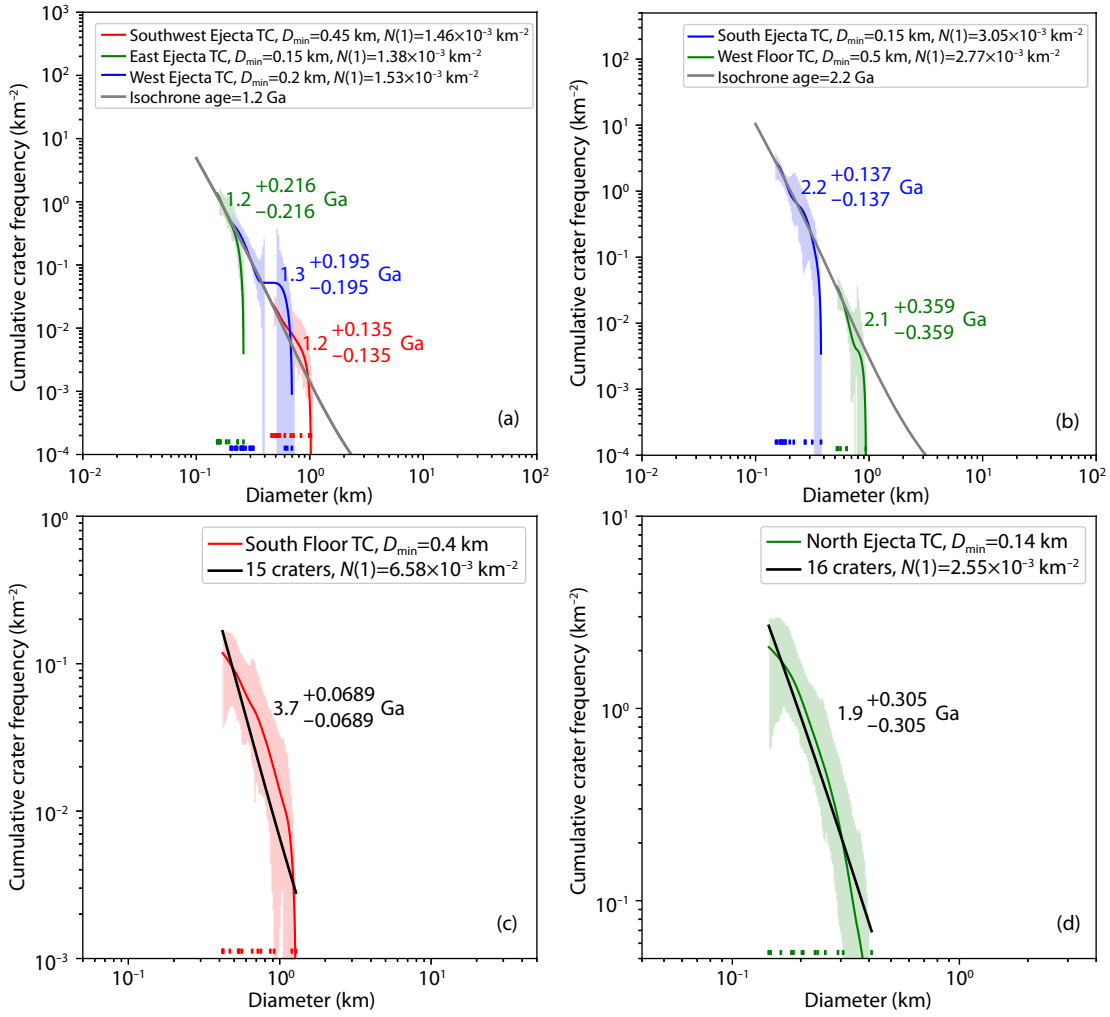

Figure 5. Cumulative crater size-frequency distribution and absolute model ages for the seven populations of relatively small craters collected on the crater floor and ejecta deposits of Finsen. The names of the counting areas correspond to those shown in Figure 3. Shaded colors are the errors for the crater size-frequency distributions.

away from the northern rim of Alder, and we are cautious that the crater floor of Alder might also be affected by Finsen's ejecta (Figure 6a). On the other hand, Alder is much more degraded than Finsen, as the melt sheets formed by Finsen are still preserved on the crater terraces (Figure 3), but those formed by Alder are not recognizable. Instead, numerous secondaries are observed overlapping Alder's ejecta deposits (Figure 7). Therefore, the heavy topographic degradation and large abundance of superposed secondaries at Alder prohibit us from using populations of small craters to estimate the model ages. In total, three areas on the continuous ejecta deposits and the entire crater floor are selected to investigate the absolute model age of Alder (Figures 6 and 7).

The absolute ages modeled for the four populations of impact craters collected at Alder are shown in Figure 8. Considering error bars, ejecta on the southern ejecta (Figure 8d) is significantly older and that on the crater floor is significantly younger (Figure 8b). The ages are clustered around ~3.9 Ga with a much smaller range than the 11 ages derived for Finsen (Figure 5). As such, the modeled ages of Alder are uniformly larger than 3.8 Ga.

4. Discussion

4.1 Age Relationships Between the Mare Basalts in Von Kármán and the Alder and Finsen Craters

4.1.1 Inconsistencies in ages modelled for different crater populations

For both Finsen and Alder, the absolute ages modelled for the different crater populations exhibit statistically significant differences (Figures 4, 5 and 8). The crater counts have strictly followed standard technical requirements (Michael and Neukum, 2010; Xiao ZY and Strom, 2012; Wang YC et al., 2020), so that each of the crater populations collected was designed to represent the age of the target crater.

Considering error bars, 5 of the 11 crater populations collected on both the floor and ejecta deposits of Finsen are clustered around 2.0 Ga (Figures 4c, 4d, 5d); 2 are close to ~3 Ga (Figures 4a and 4b); 3 are around ~1.2 Ga (Figure 5a); and 1 is ~3.7 Ga (Figure 5c). The 3 crater populations collected on the floor yield model ages of 3.0 Ga (Figure 4a), 2.1 Ga (Figure 5b), and 3.7 Ga (Figure 5c), indic-

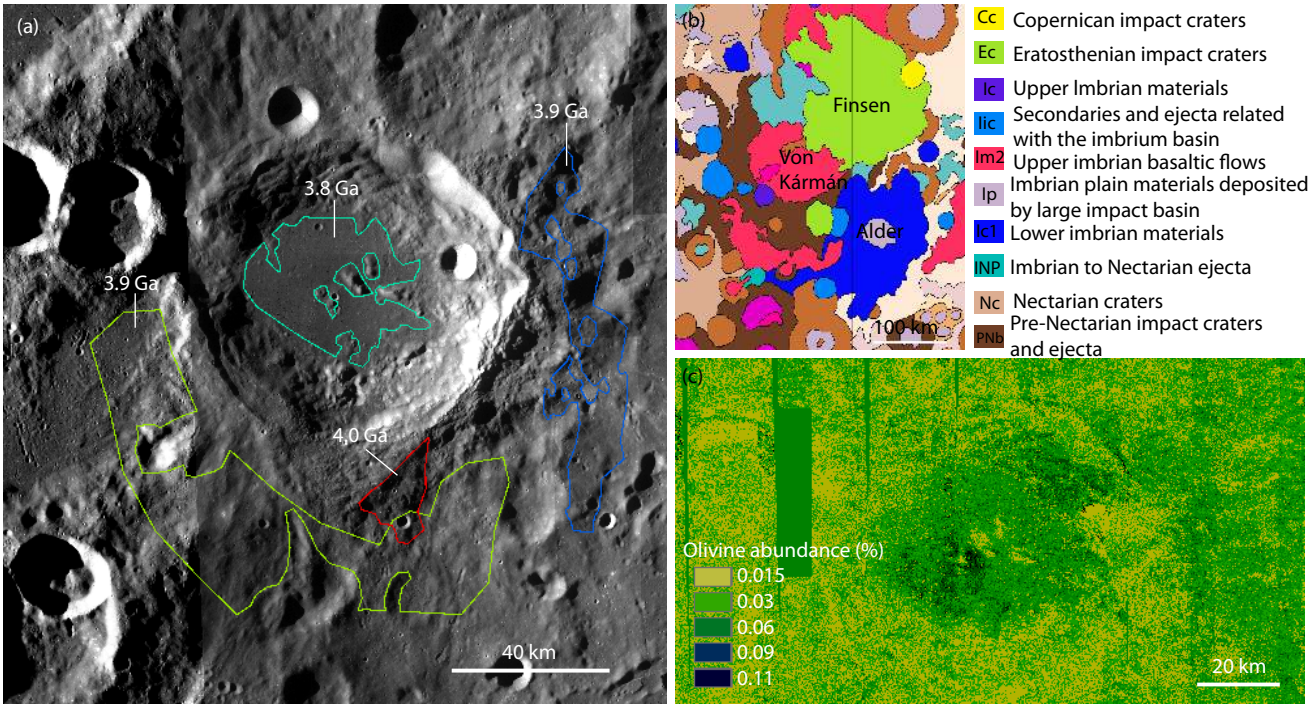

Figure 6. Morphological context of the Alder crater and the counting areas. (a) The four counting areas on the floor and continuous ejecta deposits of Alder are marked in different colors. (b) Geologic map for the area of interest around the landing site (Fortezzo et al., 2020). Stratigraphic units with different colors are explained in the figure legend. (c) Contents of olivine within and around the Alder crater derived from the Kaguya Multiband Imager (Lemelin et al., 2016).

ating a significantly non-random spatial distribution. Figure 2e shows that on the crater floor of Finsen, craters larger than 0.8 km are obviously clustered at the southeast, where the 3.7 Ga model age was derived (Figures 3h and 5c). The eastern crater floor is completely depleted of craters larger than 0.8 km (Figure 2e). However, when employing a prevalent algorithm to estimate the spatial distribution of impact craters (Michael et al., 2012), the statistical test does not show obvious clustering for the $D > 0.8$ km population (Figure S1 in the appendices). This echoes a previous test, which showed that the spatial distribution algorithms were not accurate (Xiao ZY and Werner, 2015). Our observations suggest that the $D > 1.1$ km crater population on the crater floor is heavily contaminated by background secondaries that cannot be differentiated from similar-sized primaries based on morphology (Xiao ZY, 2018). Therefore, the crater densities derived do not represent the true value for the crater floor.

Notably, the 3.68 ± 0.03 Ga, ~3.5 Ga, ~3.0 Ga ages of Finsen reported by Ivanov et al. (2018), Gou et al. (2020), and Lu et al. (2021), respectively, were all located on the crater floor. Of the four melt pools investigated on the southern rim of the Finsen crater, three exhibit clustered model ages around 1.2 Ga (Figure 5a), while the remaining one is ~2.0 Ga (Figure 5b). We do not have an explanation for the 1.2 Ga age, which is substantially younger than the majority of ages (i.e., ~2.0 Ga). Normally, crater populations that are ~2.0 Ga and younger have not reached an equilibrium state at $D > 0.2$ km (Xiao ZY and Werner, 2015), so the small ages are not due to crater obliteration, as demonstrated by their sparse spatial distribution. Contamination by secondaries is serious at smaller diameters, as shown by obvious secondaries chains at smaller diameters (Figure 3). However, contamination by background secondaries would cause densities larger than the average value, which is inconsistent with the smaller densities observed. Two possible explanations exist, but we are not able to find evidence to confirm or exclude either: (1) the Finsen impact was accompanied by immediate but uneven deposition of self-secondaries (Xiao ZY et al., 2016), such that a quick equilibrium was achieved on the melt pools that would have been otherwise impossible on normal mare surfaces (Xiao ZY and Werner, 2015); (2) as evidenced by the numerous impact rays that pass the southern rim of Finsen (Figure 1b), post-impact resurfacing by distal ejecta might have occurred on the southern rim of Finsen, which would have preferentially removed some of the small crater populations there.

The inconsistencies in the four ages modelled for Alder are relatively small, but still statistically significant (Figure 8). Past and current geology maps both assigned a stratigraphic age of Early Imbrian (i.e., 3.85–3.75 Ga; Stöffler et al., 2006) for the Alder impact, and the floor materials were mapped as younger basin ejecta that have a stratigraphic age of Imbrian (Figure 6b). The content of olivine mapped by the Kaguya Multiband Imager (Lemelin et al., 2016) shows that the flat floor, northeastern crater wall, and eastern ejecta deposits of Alder all exhibit an elevated abundance compared to the surrounding materials (Figure 6c). Morphology study does not reveal potential volcanic deposits on the floor, suggesting that the olivine-rich materials might be distal ejecta that postdate Alder. Therefore, the 3.8 Ga age derived for the crater floor is consistent with a partial resurfacing event by distal ejecta (Robbins, 2014). The counting area on the southern ejecta

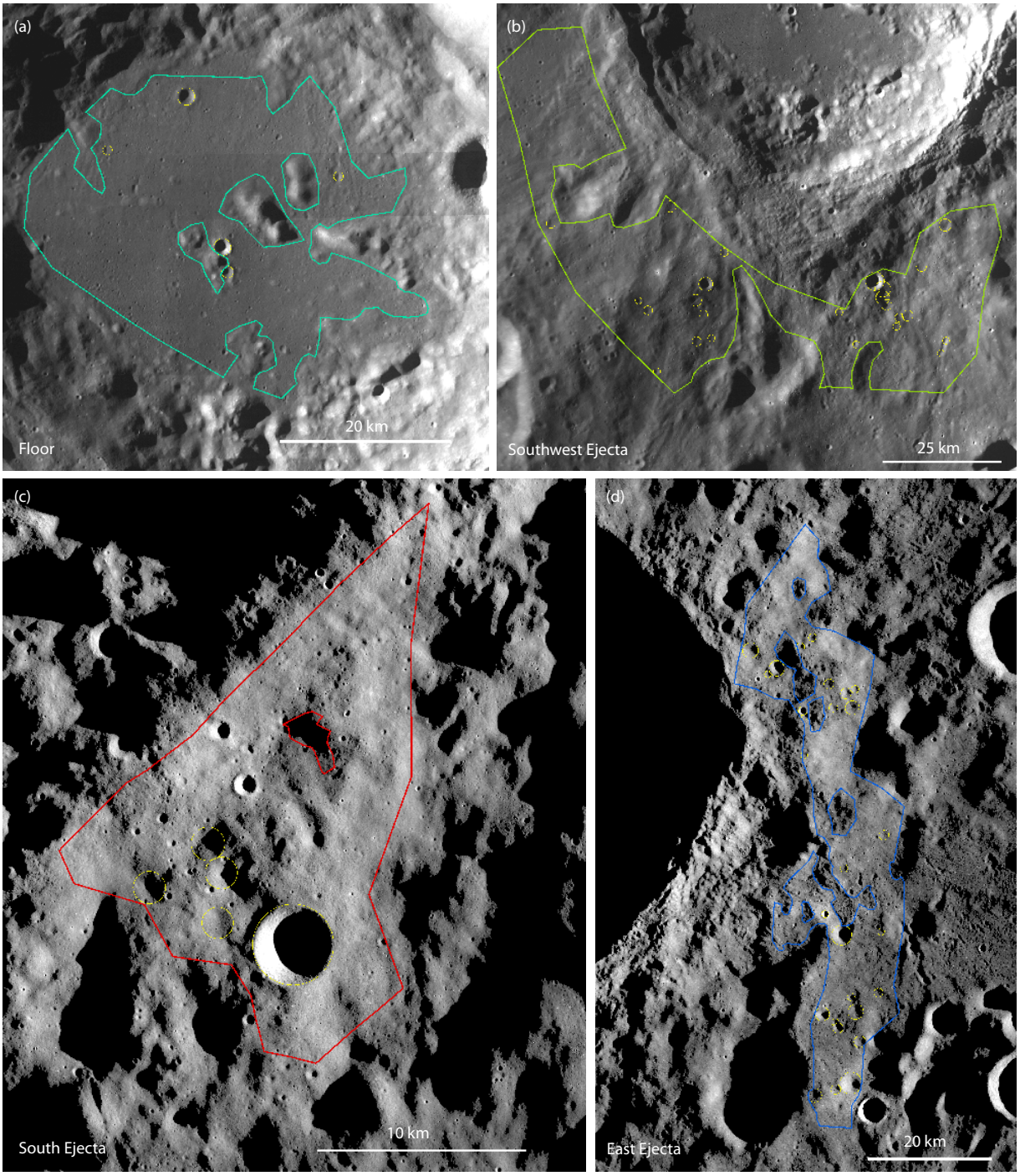

Figure 7. Detailed morphology of the 4 counting areas selected within and around Alder. The color and name of the counting areas correspond to those shown in Figure 6. Yellow circles in each panel mark the location of craters that are used to estimate the crater densities.

deposits (Figure 7c) has a model age of ~4.0 Ga, and the largest crater collected is ~4 km, which is 1/4 of the width of the counting area. The effect of small sizes of counting areas on age determination might be a reason for the slightly-larger density derived (Van Der Bogert et al., 2015).

4.1.2 Alder is older than the mare basalts on the floor of Von Kármán

The mare basalts on the floor of Von Kármán have been rigorously constrained via crater counts on three small areas and also the entire floor, yielding a robust age of ~3.6 Ga (Huang J et al., 2018). Within error bars, this value is consistent with both earlier (Pasckert et al., 2015) and later (Ling ZC et al., 2019) independent determinations. For comparison, here we have placed a solid constraint on the maximum and minimum model ages for Finsen and Alder, respectively, which are ~2 Ga and ~3.9 Ga according to the chronology function of Robbins (2014). Therefore, the debate about whether or not the Alder crater has contributed ejecta to

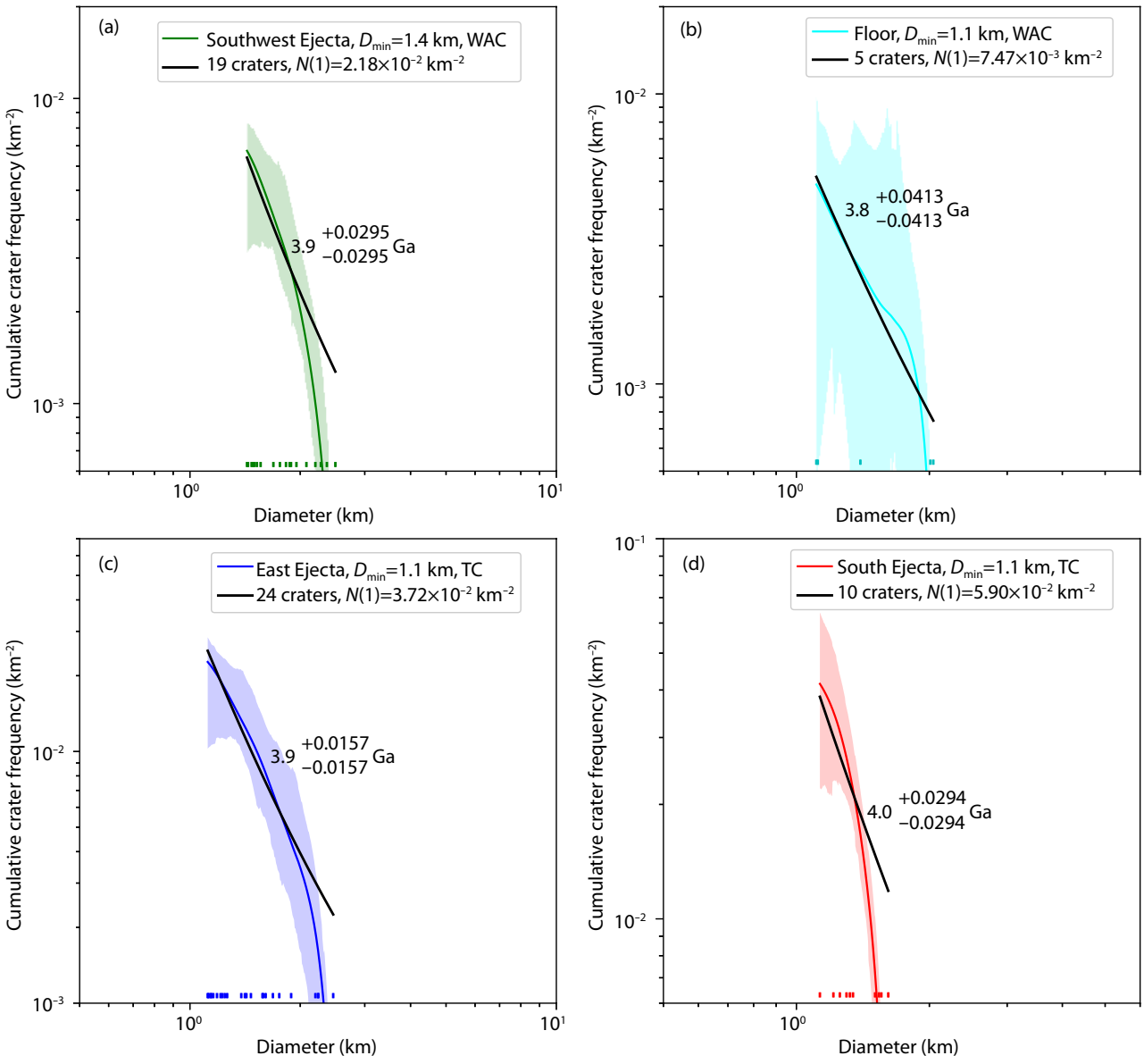

Figure 8. Cumulative crater size-frequency distribution and absolute model ages for the four populations of craters collected on the crater floor and ejecta deposits of Alder. The names of the counting areas correspond to those shown in Figure 7. Shaded colors are the errors for the crater size-frequency distributions.

the mare surface in Von Kármán can be settled.

4.2 Indications to Interpretations of Scientific Data Returned by the Yutu-2 Rover

The surface topography at the landing site was once regarded as critical evidence to support that Alder was older than the mare basalts beneath the landing site (Di KC et al., 2019). The mare surface on the floor of Von Kármán is uneven in elevation, and topographic highs and lows are common (Figure 1c; see also Lai JL et al., 2020). For example, the landing site is located on a relatively high elevation area, believed to be caused by ejecta delivered from Alder. Finsen's secondaries are heavily degraded on the floor of Von Kármán, but the northeast to southwest lineations are still well-preserved (Figure 2b). If Alder were indeed younger than the mare basalts and Finsen were formed ~3.5 Ga ago (Gou S et al., 2020), secondaries delivered by Alder should be similarly obvious on the floor of Von Kármán, considering the very small age difference (<100 Ma) between Finsen and Alder. However, no topographic traces of Alder's ejecta are visible at the landing site (Figure 2c). Moreover, without obvious ejecta deposition, the surface topography of lunar mare basalts can be uneven due to post-volcanism modification, which is a common phenomenon on the Moon. For example, the arbitrary example shown in Figure 9 is a normal mare unit that is located to the north of the Timocharis crater.

After reviewing recent advances in the local stratigraphy at the Chang'E-4 landing site, this work pins down the age relationship between Alder and the mare basalts at the landing site. The result

confirms earlier orbital observations (Huang J et al., 2018; Ling ZC et al., 2019) and supports past and recent geologic maps with quantified model ages. Implications of the results to the interpretation of data obtained by Yutu-2 await further studies, but we mention two immediate indications here: (1) for the post-mare deposits, the lunar penetrating radar would not detect substantial ejecta delivered by Alder; and (2) for the surface regolith detected by the Yutu-2 rover, the reflectance spectra obtained contain little information about Alder's ejecta.

This result leaves a question: Besides Finsen, which craters are the other provenances of materials in the post-mare deposits? Theoretical predictions suggest that Finsen's ejecta should have dominated the post-mare ejecta, which is on the order of ~8 m (Huang J et al., 2018; Lai JL et al., 2020). However, the lunar penetrating radar resolves post-mare deposits up to ~40 m thick (Lai JL et al., 2020; Li CL et al., 2020). More systemic work is warranted on the possible contributors of distal ejecta to the landing site. On the other hand, the ballistic sedimentation model that was used to predict ejecta thickness was built on empirical and limited observations, and the predictions may be biased compared to real world impacts, such as complexities caused by various impact angles and pre-impact topography.

5. Conclusion

We perform rigorous crater statistics for different populations of impact craters that are superposed on various ejecta facies of the Finsen and Alder crater. The results are cross-compared to check replicability and reliability. Together with the revealed heterogeneous modification history of the different facies, discrepancies in crater densities are analyzed, concurring in the significant contribution of uneven depositions of background secondaries and resurfacing by distal ejecta. Compared to the model age of mare basalts in the floor of Von Kármán, our results unambiguously show that Alder is older than the basalts. Thus, their geological signature is not recorded in the surface topography, nor in subsurface structures revealed by the lunar penetrating radar, nor in the reflectance spectra obtained by the Yutu-2 rover. While this study has reshaped the possible provenances of the post-mare ejecta deposit in Von Kármán, we appeal for more focused studies on the post-mare impact history around the impact site.

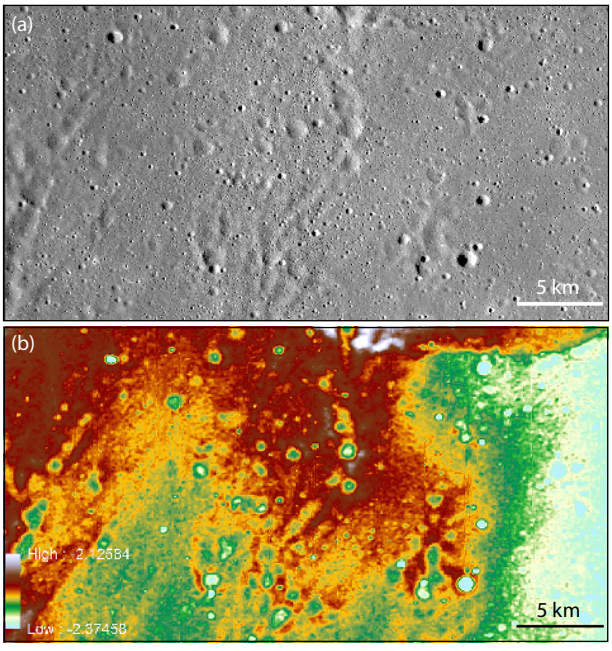

Figure 9. Mare surface on the Moon frequently exhibits uneven elevations, which are not obviously correlated with ejecta deposits. A nearside mare unit (central coordinates of the frame are 28.6°N, 12.0°W) close to the Timocharis crater is used here as an example, and such phenomena are not rare on the Moon. (a) A Kaguya Terrain Camera mosaic shows the general morphology of the mare units, where many degraded secondaries are visible. (b) SLDEM shows the regional topography of the mare unit, which features uneven elevations, but no obvious ejecta deposits are associated with the high topography. The unit of elevation here is kilometer.

Supplementary Materials

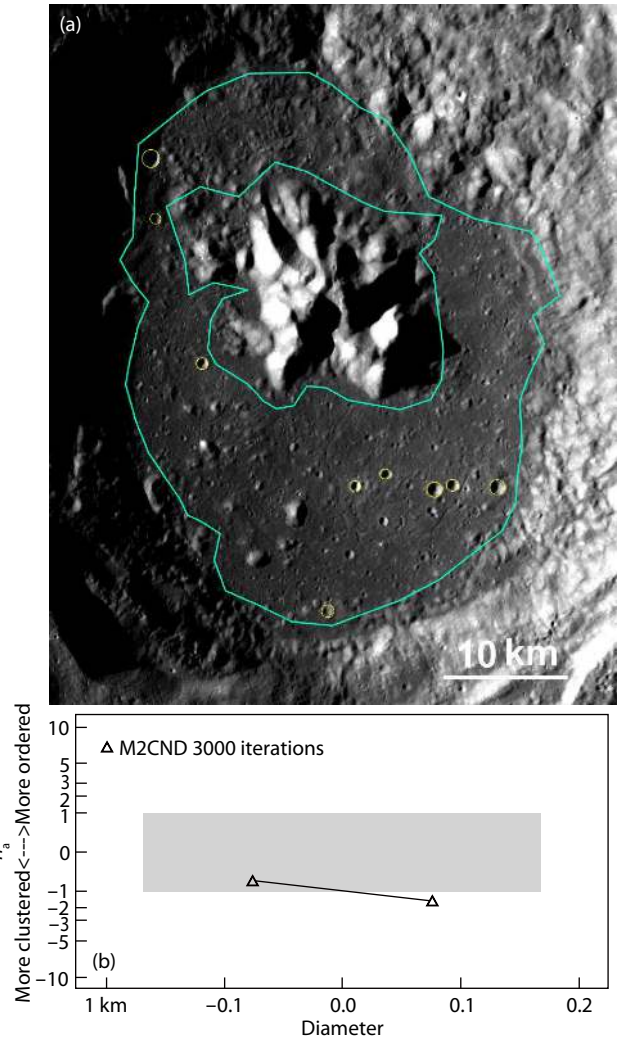

Figure S1. (a) Crater counts on the crater floor of Finsen. (b) The spatial distribution of craters larger than 1.1 km collected on the floor of Finsen as represented by the standard deviation of adjacent area (SDAA). Using this algorithm (Michael et al., 2012), the spatial distribution of the collected craters is not significant different from a random distribution.

Table S1. ID of imagery data used in this study.

Figure ID	Image ID	Pixel scale
Figure 1a	LROC_WAC_Farside_Lowsun	100 m/pixel
Figure 1b	Clem_mineral_ration_200m	200 m/pixel
Figure 1c	SLDEM2015_512_60S_30S_135_180	59 m/pixel
Figure 2a	M118681152M	111 m/pixel
Figure 2b	M118681152M	111 m/pixel
Figure 2c	M118681152M	111 m/pixel
Figure 2d	M118681152M	111 m/pixel
Figure 2e	M118681152M	111 m/pixel
Figure 3a	M118681152M	111 m/pixel
Figure 3b	TCO_MAP_04_S42E177S45E180SC	7.4 m/pixel
Figure 3c	TCO_MAP_04_S42E177S45E180SC	7.4 m/pixel
Figure 3d	TCO_MAP_04_S42E177S45E180SC	7.4 m/pixel
Figure 3e	TCO_MAP_04_S42E177S45E180SC	7.4 m/pixel
Figure 3f	TCO_MAP_04_S42E177S45E180SC	7.4 m/pixel
Figure 3g	TCO_MAP_02_S42E177S45E180SC	7.4 m/pixel
Figure 3h	TCO_MAP_02_S42E177S45E180SC	7.4 m/pixel
Figure 6a	M118640443M	75 m/pixel
	M118653839M	75 m/pixel
	M118660799M	75 m/pixel
	M118667400M	75 m/pixel
	M118681152M	78 m/pixel
Figure 6c	Lunar_Kaguya_MIMap_MineralDeconv	
	_OlivinePercent_50N50S	
Figure 7a	M118653839M	75 m/pixel
Figure 7b	M118660799M	75 m/pixel
	M118667400M	75 m/pixel
Figure 7c	TCO_MAP_04_S48E177S51E180SC	7.4 m/pixel
Figure 7d	TCO_MAP_04_S48E174S51E177SC	7.4 m/pixel
Figure 9a	TCO_MAP_04_N27E345N30E348SC	7.4 m/pixel
	TCO_MAP_04_N27E348N30E351SC	
Figure 9b	SLDEM2015_512_00N_30N_315_360	59 m/pixel

Table S2. Information of the counting areas performed in this study.

Counting areas	Central Latitude(°N)	Central Longitudes (°E)	Area (km^2)
Finsen-Southwest Ejecta	−43.6	−179.5	598.2
Finsen-North Ejecta	−43.6	−178.2	7.1
Finsen-West Ejecta	−43.7	−178.4	51.4
Finsen-South Ejecta	−43.9	−178.12	6.6
Finsen-East Ejecta	−43.8	−177.9	8.1
Finsen-West Floor	−42.5	−178.3	167.8

Continued from Table S2

Counting areas	Central Latitude(°N)	Central Longitudes (°E)	Area (km^2)
Finsen-South Floor	−42.3	−177.8	127
Finsen-Ejecta 1	−44.3	−177.5	2698.7
Finsen-Ejecta 2	−43.8	−178.1	1006.5
Finsen-Ejecta 3	−43.8	−178.1	1447.8
Finsen-Floor	−42.3	−177.8	822
Alder-Southwest Ejecta	−50.6	−179.2	2819.5
Alder-East Ejecta	−49	−174.8	1058.2
Alder-South Ejecta	−50.4	−177.4	240.8
Alder-Floor	−48.6	−178.3	1026

Table S3. Basic information of base images used for the crater counts.

Counting areas	Base image	Pixel scale	Angle (°)
Finsen-North Ejecta	TCO_MAP_04_S39E 177S42E180SC	7.4 m/pixel	
Finsen-West Ejecta	TCO_MAP_04_S42E 177S45E180SC		
Finsen-South Ejecta			
Finsen-East Ejecta			
Finsen-Southwest Ejecta			
Finsen-West Floor	TCO_MAP_02_S42E 177S45E180SC	7.4 m/pixel	
Finsen-South Floor			
Finsen-Ejecta 1	M118681152M	75 m/pixel	76.2
Finsen-Ejecta 2			
Finsen-Ejecta 3			
Finsen-Floor			
Alder-Floor	M118640443M	75 m/pixel	75.2
Alder-Southwest Ejecta	M118653839M	75 m/pixel	77.9
	M118660799M	75 m/pixel	75.2
	M118667400M	75 m/pixel	77.8
	M118681152M	78 m/pixel	76.2
Alder-East Ejecta	TCO_MAP_04_S45E 174S48E177SC	7.4 m/pixel	
Alder-South Ejecta	TCO_MAP_04_S48E 174S51E177SC		
	TCO_MAP_04_S45E 177S48E180SC		
	TCO_MAP_04_S48E 177S51E180SC		

Acknowledgments

This work is supported by the B-type Strategic Priority Program of the Chinese Academy of Sciences (Grant No. XDB41000000), the Science and Technology Development Fund of Macau (0042/2018/A2), the National Natural Science Foundation of China (No. 41773063), and the pre-research Project on Civil Aerospace Technologies (No. D020201 and D020202) that is funded by Chinese National Space Administration. The two reviewers are thanked for their suggestions and comments.

References

Barker, M. K., Mazarico, E., Neumann, G. A., Zuber, M. T., Haruyama, J., and Smith, D. E. (2016). A new lunar digital elevation model from the Lunar Orbiter Laser Altimeter and SELENE Terrain Camera. *Icarus*, *273*, 346–355. https://doi.org/10.1016/j.icarus.2015.07.039

Di, K. C., Zhu, M. H., Yue, Z. Y., Lin, Y. T., Wan, W. H., Liu, Z. Q., Gou, S., Liu, B., Peng, M., … Xue, B. (2019). Topographic Evolution of Von Kármán Crater Revealed by the Lunar Rover Yutu-2. *Geophys. Res. Lett.*, *46*(22), 12764–12770. https://doi.org/10.1029/2019GL085252

Ding, C. Y., Xiao, Z. Y., Wu, B., Li, Y., Prieur, N. C., Cai, Y. Z., Su, Y., and Cui, J. (2020). Fragments delivered by secondary craters at the Chang'e-4 landing site. *Geophys. Res. Lett.*, *47*(7), e2020GL087361. https://doi.org/10.1029/2020GL087361

Eliason, E. M., McEwen, A. S., Robinson, M. S., Lee, E. M., Becker, T., Gaddis, L., Weller, L. A., Isbell, C. E., Shinaman, J. R., … Malaret, E. (1999). Digital processing for a global multispectral map of the moon from the clementine UVVIS imaging instrument. In *Proceedings of the 30th Annual Lunar and Planetary Science Conference*. Houston.

Fa, W. Z., Zhu, M. H., Liu, T. T., and Plescia, J. B. (2015). Regolith stratigraphy at the Chang'E-3 landing site as seen by lunar penetrating radar. *Geophys. Res. Lett.*, *42*(23), 10179–10187. https://doi.org/10.1002/2015GL066537

Fortezzo, C. M., Spudis, P. D., and Harrel, S. L. (2020). Release of the digital unified global geologic map of the moon at 1: 5, 000, 000-Scale. In *Proceedings of the 51nd Lunar and Planetary Science Conference*. Houston, TX: Lunar and Planetary Institute.

Gou S., Yue, Z. Y., Di, K. C., Cai, Z. C., Liu, Z. Q., and Niu, S. L. (2020). Absolute model age of lunar Finsen crater and geologic implications. *Icarus*, *354*, 114046. https://doi.org/10.1016/j.icarus.2020.114046

Haruyama, J., Matsunaga, T., Ohtake, M., Morota, T., Honda, C., Yokota, Y., Torii, M., Ogawa, Y., and LISM Working Group. (2008). Global lunar-surface mapping experiment using the Lunar Imager/Spectrometer on SELENE. *Earth Planets Space*, *60*(4), 243–255. https://doi.org/10.1186/BF03352788

Hawke, B. R., Blewett, D. T., Lucey, P. G., Smith, G. A., Bell III, J. F., Campbell, B. A., and Robinson, M. S. (2004). The origin of lunar crater rays. *Icarus*, *170*, 1–16. https://doi.org/10.1016/j.icarus.2004.02.013

Huang, J., Xiao, Z. Y., Flahaut, J., Martinot, M., Head, J., Xiao, X., Xie, M. G., and Xiao, L. (2018). Geological characteristics of Von Kármán Crater, northwestern South Pole-Aitken basin: Chang'E-4 landing site region. *J. Geophys. Res.: Planets*, *123*(7), 1684–1700. https://doi.org/10.1029/2018JE005577

Huang, J., Xiao, Z. Y., Xiao, L., Briony, H., Hu, X. Y., Lucey, P., Xiao, X., Zhao, S. Y., Qian, Y. Q., … Xie, J. F. (2020). Diverse rock types detected in the lunar South Pole-Aitken Basin by the Chang'E-4 lunar mission. *Geol. Soc. Am.*, *48*(7), 723–727. https://doi.org/10.1130/G47280.1

Ivanov, M. A., Hiesinger, H., Van Der Bogert, C. H., Orgel, C., Pasckert, J. H., and Head, J. W. (2018). Geologic history of the northern portion of the South Pole-Aitken Basin on the moon. *J. Geophys. Res.: Planets*, *123*(10), 2585–2612. https://doi.org/10.1029/2018JE005590

Lai, J. L., Xu, Y., Zhang, X. P., Xiao, L., Yan, Q., Meng, X., Zhou, B., Dong, Z. H., and Zhao, D. (2019). Comparison of dielectric properties and structure of lunar regolith at Chang'e-3 and Chang'e-4 landing sites revealed by ground-penetrating radar. *Geol. Res. Lett.*, *46*(12), 12783–12793. https://doi.org/10.1029/2019GL084458

Lai, J. L., Xu, Y., Bugiolacchi, R., Meng, X., Xiao, L., Xie, M. G., Liu, B., Di, K. C., Zhang, X. P., … Xu, L. Y. (2020). First look by the Yutu-2 rover at the deep subsurface structure at the lunar farside. *Nature Communications*, *11*(1), 3426. https://doi.org/10.1038/s41467-020-17262-w

Lemelin, M., Lucey, P. G., Gaddis, L. P., Hare, T., and Ohtake, M. (2016). Global map products from the kaguya multiband imager at 512 ppd: minerals, FeO, and OMAT. In *Proceedings of the 47th Lunar and Planetary Science Conference*. The Woodlands, Texas.

Li, C. L., Liu, D. L., Liu, B., Ren, X., Liu, J. J., He, Z. P., Zuo, W., Zeng, X. G., Xu, R., … Ouyang, Z. Y. (2019). Chang'E-4 initial spectroscopic identification of lunar far-side mantle-derived materials. *Nature*, *569*(7756), 378–382. https://doi.org/10.1038/s41586-019-1189-0

Li, C. L., Su, Y., Pettinelli, E., Xing, S. G., Ding, C. Y., Liu, J. J., Ren, X., Lauro, S. E., Soldovieri, F., … Zhang, H. B. (2020). The Moon's farside shallow subsurface structure unveiled by Chang'E-4 lunar penetrating Radar. *Sci. Adv.*, *6*(9), eaay6898. https://doi.org/10.1126/sciadv.aay6898

Lin, H. L., He, Z. P., Yang, W., Lin, Y. T., Xu, R., Zhang, C., Zhu, M. H., Chang, R., Zhang, J. H., … Zou, Y. L. (2020). Olivine-norite rock detected by the lunar rover Yutu-2 likely crystallized from the SPA-impact melt pool. *Natl. Sci. Rev.*, *7*(5), 913–920. https://doi.org/10.1093/nsr/nwz183

Ling, Z. C., Jolliff, B. L., Liu, C. Q., Bi, X. Y., Liu, L., Qiao, L., Li, B., Zhang, J., Fu, X. H., and Liu, J. Z. (2018). Composition, mineralogy, and chronology of mare basalts in Von Kármán crater: a candidate landing site of Chang'E-4. In *Proceedings of the 49th Lunar and Planetary Science Conference*. The Woodlands, Texas.

Ling, Z. C., Qiao, L., Liu, C. Q., Cao, H. J., Bi, X. Y., Lu, X. J., Zhang, J., Fu, X. H., Li, B., and Liu, J. Z. (2019). Composition, mineralogy and chronology of mare basalts and non-mare materials in Von Kármán crater: landing site of the Chang'E–4 mission. *Planet. Space Sci.*, *179*, 104741. https://doi.org/10.1016/j.pss.2019.104741

Lu, Y., Wu, Y. Z., Michael, G. G., Ma, J. S., Cai, W., and Qin, N. N. (2021). Chronological sequence of Chang'E-4 landing zone within Von Kármán crater. *Icarus*, *354*, 114086. https://doi.org/10.1016/j.icarus.2020.114086

Ma, P., Sun, Y. X., Zhu, M. H., Yang, Y. Z., Hu, X. Y., Jiang, T., Zhang, H., Lucey, P. G., Xu, R., … Lin, H. Y. (2020). A plagioclase-rich rock measured by Yutu-2 Rover in Von Kármán crater on the far side of the Moon. *Icarus*, *350*, 113901. https://doi.org/10.1016/j.icarus.2020.113901

McEwen, A. S., and Bierhaus E. B. (2006). The importance of secondary cratering to age constraints on planetary surfaces. *Annu. Rev. Earth Planet.*, *34*, 535–567. https://doi.org/10.1146/annurev.earth.34.031405.125018

Melosh, H. J., Kendall, J., Horgan, B., Johnson, B. C., Bowling, T., Lucey, P. G., and Taylor, G. J. (2017). South Pole–Aitken basin ejecta reveal the Moon's upper mantle. *Geology*, *45*(12), 1063–1066. https://doi.org/10.1130/G39375.1

Michael, G. G., and Neukum, G. (2010). Planetary surface dating from crater size-frequency distribution measurements: partial resurfacing events and statistical age uncertainty. *Earth Planet. Sci. Lett.*, *294*(3-4), 223–229. https://doi.org/10.1016/j.epsl.2009.12.041

Michael, G. G., Platz, T., Kneissl, T., and Schmedemann N. (2012). Planetary surface dating from crater size-frequency distribution measurements: spatial randomness and clustering. *Icarus*, *218*(1), 169–177. https://doi.org/10.1016/j.icarus.2011.11.033

Moriarty III, D. P., and Pieters, C. M. (2018). The character of South Pole - Aitken Basin: patterns of surface and sub-surface composition. *J. Geophys. Res.: Planets*, *123*(3), 729–747. https://doi.org/10.1002/2017JE005364

Neukum, G., Ivanov, B. A., and Hartmann, W. K. (2001). Cratering records in the inner solar system in relation to the lunar reference system. *Space Sci. Rev.*, *96*(1-4), 55–86. https://doi.org/10.1023/A:1011989004263

Ostrach, L. R., Robinson, M. S., Denevi, B. W., and Thomas, P. C. (2011). Effects of incidence angle on crater counting observations. In *Proceedings of the 42nd Lunar and Planetary Science Conference*.

Pasckert, J. H., Hiesinger, H., and Van Der Bogert, C. H. (2015). Small-scale lunar farside volcanism. *Icarus*, *257*, 336–354. https://doi.org/10.1016/j.icarus.2015.04.040

Pasckert, J. H., Hiesinger, H., and Van Der Bogert, C. H. (2018). Lunar farside volcanism in and around the south pole-Aitken basin. *Icarus*, *299*, 538–562.

https://doi.org/10.1016/j.icarus.2017.07.023

Potter, R. W. K., Collins, G. S., Kiefer, W. S., McGovern, P. J., and Kring, D. A. (2012). Constraining the size of the South Pole-Aitken basin impact. *Icarus*, *220*(2), 730–743. https://doi.org/10.1016/j.icarus.2012.05.032

Robbins, S. J. (2014). New crater calibrations for the lunar crater-age chronology. *Earth Planet. Sci. Lett.*, *403*, 188–198. https://doi.org/10.1016/j.epsl.2014.06.038

Robbins, S. J., Riggs, J. D., Weaver, B. P., Bierhaus, E. B., Chapman, C. R., Kirchoff, M. R., Singer, K. N., and Gaddis, L. R. (2018). Revised recommended methods for analyzing crater size-frequency distributions. *Mateoritics Planet. Sci.*, *53*(4), 891–931. https://doi.org/10.1111/maps.12990

Robinson, M. S., Brylow, S. M., Tschimmel, M., Humm, D., Lawrence, S. J., Thomas, P. C., B. W. Denevi, E. Bowman-Cisneros, J. Zerr, … Hiesinger, H. (2010). Lunar Reconnaissance Orbiter Camera (LROC) instrument overview. *Space Sci. Rev.*, *150*(1-4), 81–124. https://doi.org/10.1007/s11214-010-9634-2

Stöffler, D., Ryder, G., Ivanov, B. A., Artemieva, N. A., Cintala, M. J., and Grieve, R. A. F. (2006). Cratering history and lunar chronology. *Rev. Mineral. Geochem.*, *60*(1), 519–596. https://doi.org/10.2138/rmg.2006.60.05

Van Der Bogert, C. H., Michael, G., Kneissl, T., Hiesinger, H., and Pasckert, J. H. (2015). Effects of count area size on absolute model ages derived from random crater size-frequency distributions. In *Proceedings of the 46th Lunar and Planetary Science Conference*. The Woodlands, Texas.

Wang, Y. C., Xie, M. G., Xiao, Z. Y., and Cui, J. (2020). The minimum confidence limit for diameters in crater counts. *Icarus*, *341*, 113645. https://doi.org/10.1016/j.icarus.2020.113645

Wilhelms, D. E., Howard, K. A., and Wilshire. H. G. (1979) Geologic map of the south side of the Moon. United States Geological Survey. https://doi.org/10.3133/i1162

Wu, W. R., Wang, Q., Tang, Y. H., Yu, G. B., Liu, J. Z., Zhang, W., Ning, Y. M., and Lu, L. L. (2017). Design of Chang'E-4 lunar farside soft-landing mission. *J. Deep Space Explor.* (*in Chinese*), *4*(2), 111–117. https://doi.org/10.15982/j.issn.2095-7777.2017.02.002

Xiao, L., Zhu, P. M., Fang, G. Y., Xiao, Z. Y., Zou, Y. L., Zhao, J. N., Zhao, N., Yuan, Y. F., Qiao, L., … Gao, Y. Z. (2015). A young multilayered terrane of the northern Mare Imbrium revealed by Chang'E-3 mission. *Science*, *347*(6227), 1226–1229. https://doi.org/10.1126/science.1259866

Xiao, Z. Y., and Strom R. G. (2012). Problems determining relative and absolute ages using the small crater population. *Icarus*, *220*(1), 254–267. https://doi.org/10.1016/j.icarus.2012.05.012

Xiao, Z. Y., Zeng, Z. X., Ding, N., and Molaro, J. (2013). Mass wasting features on the moon–how active is the lunar surface? . *Earth Planet Sci. Lett.*, *376*, 1–11. https://doi.org/10.1016/j.epsl.2013.06.015

Xiao, Z. Y., and Werner S. C. (2015). Size-frequency distribution of crater populations in equilibrium on the moon. *J. Geophys. Res.: Planets*, *120*(12), 2277–2292. https://doi.org/10.1002/2015JE004860

Xiao, Z. Y., Prieur, N. C., and Werner, S. C. (2016). The self-secondary crater population of the Hokusai crater on mercury. *Geophys. Res. Lett.*, *43*(14), 7424–7432. https://doi.org/10.1002/2016GL069868

Xiao, Z. Y. (2018). On the importance of self-secondaries. *Geosci. Lett.*, *5*(1), 17. https://doi.org/10.1186/s40562-018-0116-9

Zhang, J. H., Yang, W., Hu, S., Lin, Y. T., Fang, G. Y., Li, C. L., Peng, W. X., Zhu, S. Y., He, Z. P., … Ouyang, Z. Y. (2015). Volcanic history of the Imbrium basin: a close-up view from the lunar rover Yutu. *Proc. Natl. Acad. Sci. U S A*, *112*(17), 5342–5347. https://doi.org/10.1073/pnas.1503082112

Zhang, L., Li, J., Zeng, Z. F., Xu, Y., Liu, C., and Chen, S. B. (2020). Stratigraphy of the Von Kármán crater based on Chang'E-4 lunar penetrating radar data. *Geophys. Res. Lett.*, *47*(15), e2020GL088680. https://doi.org/10.1029/2020GL088680